Measurement 77 (2016) 54–66

Contents lists available at ScienceDirect

Measurement

journal homepage: www.elsevier.com/locate/measurement

Experimental evaluation of a distributed Brillouin sensing system for measuring extensional and shear deformation in rock

Behrad Madjdabadi [a,*], Benoît Valley [b], Maurice B. Dusseault [c], Peter K. Kaiser [d]

[a] Department of Civil and Environmental Engineering, University of Waterloo, Waterloo, Ontario, Canada
[b] Centre for Hydrogeology and Geothermics (CHYN), University of Neuchâtel, Neuchâtel, Switzerland
[c] Department of Earth & Environmental Sciences, University of Waterloo, Waterloo, Ontario, Canada
[d] Bharti School of Engineering, Laurentian University, Sudbury, Ontario, Canada

ARTICLE INFO

Article history:
Received 27 May 2015
Received in revised form 17 August 2015
Accepted 19 August 2015
Available online 8 September 2015

Keywords:
Brillouin frequency shift
SMARTprofile™
DiTeSt™
Spatial resolution
Displacement
Strain

ABSTRACT

Distributed Brillouin sensing systems (DBSs) have growing applications in engineering and are attracting attention in the field of underground structures, including mining. The capability for continuous measurements of strain over large distances makes DBSs a promising monitoring approach for understanding deformation field evolution within a rock mass, particularly when the sensor is installed away from excavation damaged zone (EDZ). A purpose-built fiber optic sensing cable, a vital component of DBSs, was assessed in laboratory conditions.

A test program was performed to observe DBSs response to various perturbations including strain and joint movements, including opening and shearing of joints. These tests included assessment of the strain-free cable response and the application of extensional and lateral displacement to various sensing cable lengths (strained lengths), from 1 m down to 1 cm. Furthermore, tests were done to evaluate the time-dependent behavior of the cable and to observe the effect of strain transfer using a soft host material (e.g. a soft grout) under lateral displacement.

The noise level of the DBSs range was ±77 με, determined through repeated measurements on an unstrained cable. Stretching test results showed a clear linear correlation between applied strain and Brillouin frequency shift change for all strained lengths above half the spatial resolution of the DBSs. However, for strained lengths shorter than half the spatial resolution, no strain response was measurable and this is due to the applied internal signal processing of the DBSs to detect peak Brillouin gain spectrum and noise level. The stability with time of the measurements was excellent for test periods up to 15 h.

Lateral displacement test results showed a less consistent response compared to tension tests for a given applied displacement. Although the Brillouin frequency shift change is correlated linearly with the applied displacement in tension, it shows a parabolic variation with lateral displacement. Moreover, the registered frequency response (correlated with strain) of the system decreased significantly when the sensing cable was embedded in a sand-filled tube compared with direct cable displacement.

* Corresponding author.
E-mail address: bmollaha@uwaterloo.ca (B. Madjdabadi).

http://dx.doi.org/10.1016/j.measurement.2015.08.040
0263-2241/

1. Introduction

For many years, strain measurement in various engineering contexts has been done using point sensors such as strain gages. However, in large structures, point sensors cannot easily delineate the strain field on a large scale. A recently developed monitoring device called a distributed Brillouin-based sensing systems (DBSs), in conjunction with purpose-built fiber optic sensors, can provide continuous strain measurements along the length of a cable over large distances. This characteristic makes DBSs attractive to monitor large structures such as mines where the strain field is expected to be heterogeneous. DBSs sensors can also measure the temperature at the same locations, so they are appropriate for thermoelastic cases because the strain can be independently corrected for temperature.

DBSs were first used in the late 1980s to measure local attenuation in optical fibers [1]. Since then, they have been used for monitoring in different applications including electrical power lines [2], oil and gas pipelines [3], coiled tubing [4], concrete and steel bridges [5–7], composite structures [8], embankments and dams [9], and landslide and slope stability assessment [10]. They have also been applied to the monitoring of underground excavations including shallow tunnels [11] and underground mines [12].

Apart from a few field installations, such systems have been mostly used in experimental research to evaluate a specific parameter in comparison with more conventional sensors. Several studies have addressed measurement performance when the sensor is attached or embedded in a concrete beam under deflection [13–15], or to study pre-embedded defects in steel pipelines [16], composite pipes [17], and well casing [18]. Also, in a study with the same DBS as used in this study, validation of measured bending strain was evaluated in a number of long beams made of concrete, wood, and aluminum with different sensor attachment methods [19].

Microseismic events are common in deep underground mining as the rock mass responds to excavation operations. Such events are typically located close to excavation boundaries, but there have been large seismic events distant from mined-out regions, particularly as the extraction ratio increases [20]. Apart from near-field events that are known as stress-induced events, distant events cannot easily be explained by elastic field stress changes; deformation field variations caused by gravity-driven rock block movements may be a better way of explaining these events. Hence, to understand rock mass behavior around a mine, more distant deformations must be measured, and in this regard, distributed optical fiber sensors (DOFSs) may help understanding and modeling of three-dimensional load transfer mechanisms and rock mass response.

If a DBSs is to be installed in a deep underground mine to monitor the remote deformation field, proper characterisation of the sensing system performance and limitations before field installation is necessary. This article presents results from an experimental test program on the response of a DBSs, including longitudinal extension, lateral displacement, and measurements on unstrained cable for noise level assessment.

2. Background

2.1. DBSs working principles

When light is sent through an optical fiber, scattering causes losses. A small portion of the light is back-scattered, propagating in the opposite direction of the pulsed light, and it is used for sensing purposes. Three types of light scattering happen in an optical fiber: Rayleigh, Brillouin, and Raman scattering (Fig. 1). Raman and Brillouin scattering have found great acceptance as sensing methods for distributed sensors. Both are based on the difference between the optical properties of the pulsed light and the back-scattered light. Compared to the incident light frequency, v, the Raman scattering light is shifted ±10–13 THz, whereas Brillouin scattering frequency varies by ±10–13 GHz [21]. The intensity of Raman scattering light is sensitive to temperature changes (ΔT), making it a reliable and widely used temperature sensing system.

Using a Raman system with multi-mode fibers, a resolution of 0.1 °C for ΔT and a spatial resolution of 1 m over a 8 km length is feasible [22]. However, since Brillouin scattering is based on frequency modulation, it is more accurate and stable for long-term use compared to intensity-based Raman techniques [23].

In Brillouin scattering, the scattered light reaches a peak over its spectrum at a frequency shifted from the pulsed light computed by Eq. (1), known as the Brillouin frequency shift, v_B.

$$v_B = 2nV_a/\lambda_o \tag{1}$$

Here, n is the effective refractive index of the fiber, V_a is the acoustic wave velocity of the fiber core, and λ_o is the vacuum wavelength of the incident light. V_a is dependent on temperature and density changes due to strain along the sensing fiber, as is the Brillouin frequency shift, given by Eq. (2).

$$v_B = v_{B0} + C_\varepsilon \Delta\varepsilon + C_T \Delta T \tag{2}$$

The Brillouin frequency at the initial reading at a given (T, ε) condition is v_{B0}, and $\Delta\varepsilon$ and ΔT are the strain and temperature changes at subsequent measurements.

Brillouin scattering sensing is particularly useful for strain measurements as it can provide spatial resolution of about a meter along a 50 km long fiber [24]. Measurement resolution can reach 1 °C for ΔT and 2×10^{-5} for $\Delta\varepsilon$ sensing [4].

Among available Brillouin sensing technologies, two types are more common; the first, based on spontaneous scattering, is called Brillouin Time Domain Reflectometry (BOTDR), the other is called Brillouin Time Domain Analysis (BOTDA). BOTDR requires access to one end of the sensing cable, whereas the stimulated scattering system BODTA requires access to both ends of the sensing cable [21].

In stimulated scattering, BOTDA, a weak continuous wave light called the probe beam is back propagated into one end of the fiber while an intense pumped pulse is simultaneously sent into the other end. The stimulation process, i.e. gain, becomes maximized when the frequency

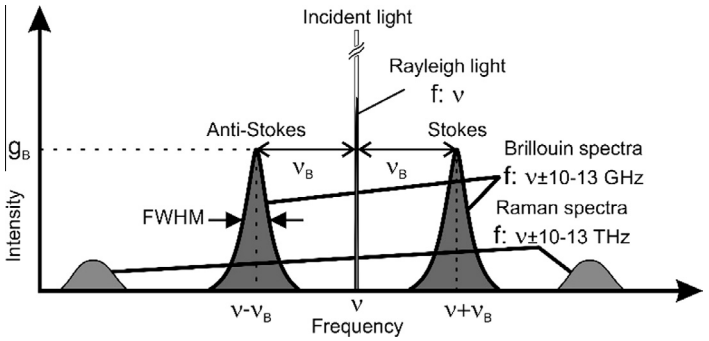

Fig. 1. Typical spectra of scattered light in optical fiber. ΔT affects both Raman and Brillouin components, whereas only strain changes the Brillouin component (modified from [21]). *FWHM* stands for the full width at half maximum.

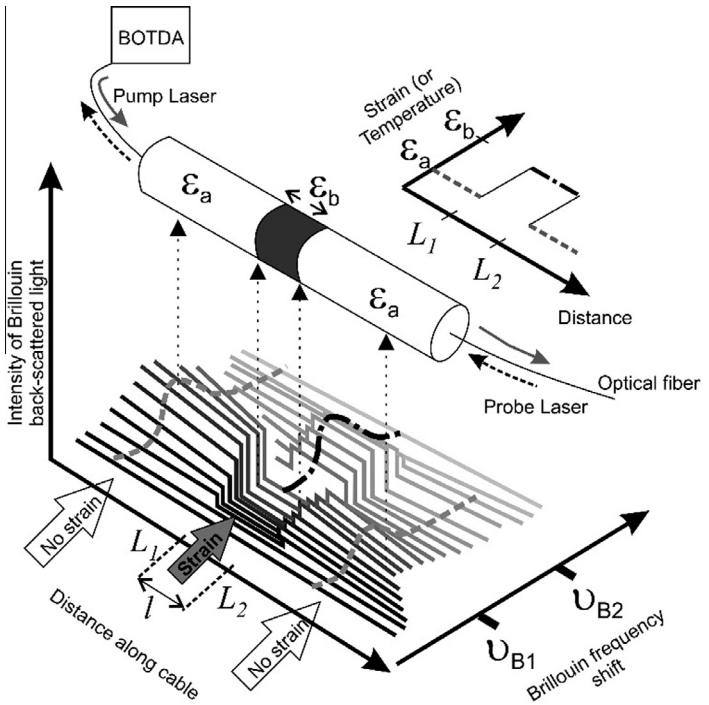

Fig. 2. Effect of strain on Brillouin gain spectrum for a BOTDA system; the Brillouin gain peaks when the frequency difference between pump and probe signals becomes equal to the local Brillouin frequency shift (modified from [21]).

Table 1
DiTeSt™ configuration used in the all measurements.

Spatial resolution L_{SR}	Sampling interval L_{SI}	Distance resolution	Frequency resolution	Frequency scan range
0.5 m	0.1 m	0.1 m	1 MHz	10.2–11.1 GHz

difference between these two beams is equal to the Brillouin frequency shift. The gain process is accomplished through monitoring the power transfer ratio from pump to probe light at certain light frequencies in a step-wise manner. The Brillouin gain spectrum can therefore be locally rebuilt when the gain as a function of frequency at any individual sampling point along the fiber optic is analysed, as shown in Fig. 2.

The DBSs used for the present study is a BOTDA commercially known as DiTeSt™ manufactured by Omnisens SA. Table 1 gives the DiTeSt™ configuration used for all measurements in this study.

A special fiber optic cable, called SMARTprofile™ made by Smartec, is used as the sensing cable. The SMARTprofile™ has two separate ε–T sensor pairs, S1–T1 and S2–T2. Strain sensors are directly embedded in the polyethylene

(PE) thermoplastic jacket in a way that any external force on the jacket fully transfers to the fiber optic sensor. The temperature sensors are placed in a tube before embedding in the PE jacket to provide a strain-free condition, so they are only affected by ΔT, not $\Delta\varepsilon$.

2.2. Spatial resolution and strained length

The sensing system shows sensitivity to ΔT and $\Delta\varepsilon$ at any location along the sensing cable; however, the Brillouin frequency shift is measured at discrete points (sampling intervals – SI) spaced at a constant interval (L_{SI} – Table 1). The location of each discrete point along the cable, x_i, is a linear function of the sampling interval, L_{SI}, the number of points, n, and the coordinate of the first point, x_0. The measurement at each point is computed through averaging of frequency measurement at all sampling points over the spatial resolution. The spatial resolution, L_{SR}, of a DBS system is controlled by the pulse width and corresponds to a fiber length below which the strain is not registered with complete available accuracy [6]. According to Table 1, L_{SR} = 50 cm includes five sampling points of L_{SI} = 10 cm.

Three different strained section lengths, l, relative to the spatial resolution, L_{SR} are given as examples to better understand the relationship between the spatial resolution and the strained length. These scenarios are (1) $l > L_{SR}$, Fig. 3a, (2) $L_{SR}/2 < l < L_{SR}$, Fig. 3b, and (3) $l < L_{SR}/2$, Fig. 3c. Three cases are possible in each scenario. Case 1 in all scenarios is encountered when the sampling point is in the strain-free section and located at least $L_{SR}/2$ away from the edges of the strained section. In this case no frequency change is registered at the sampling point. In Case 2 of all scenarios the sampling points is within $\pm L_{SR}/2$ m of the edge of the strained section and thus the spatial resolution window partially covers both the strain-free and the strained sections. Therefore it is expected that the Brillouin frequency shift change, Δv_B, will show a linear variation over sampling points within this window, indicated as the sloped portion of the frequency response in Fig. 3a–b. This linear trend would be proportional to the strained length ratio within L_{SR}, discussed in more detail in Section 3.2.3.

For scenario 1, Case 3 corresponds to all sampling points that are within the strained section located at a distance at least $\pm L_{SR}/2$ away from the section ends. In other words, all the sampling points over the spatial resolution interval are strained, so that these points should register a Δv_B which gives the closest strain to the applied strain, shown as the flat maximum frequency response in Fig. 3a. In contrast to scenario 1, in Case 2 for the second scenario not all but the majority of the sampling points within the spatial resolution interval are strained, i.e. since the length covered by the spatial resolution is larger than

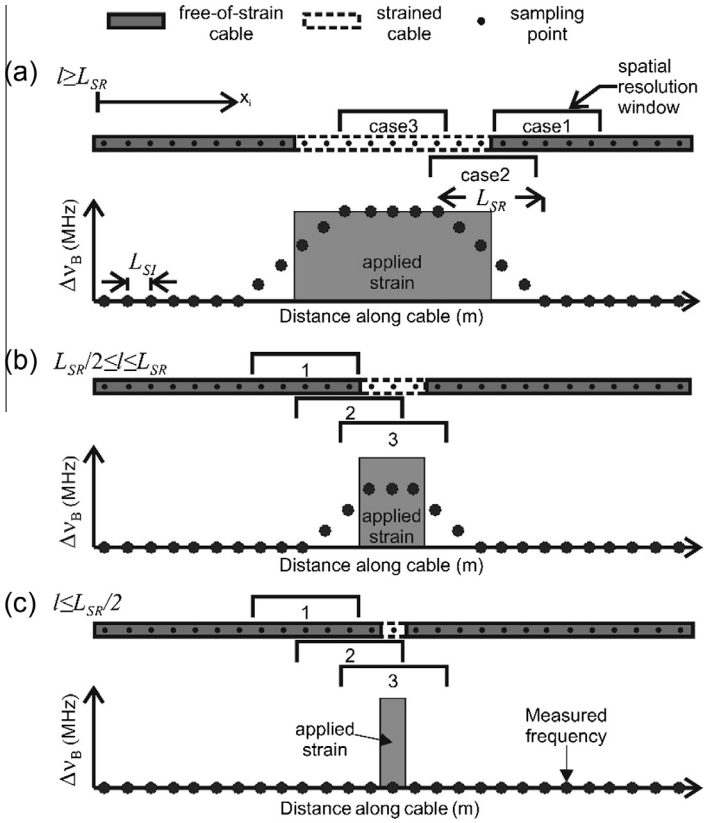

Fig. 3. Effect of length of strained section, l, with respect to spatial resolution, L_{SR}; no frequency response is expected for $l \leqslant L_{SR}/2$, linear variation of frequency change with strained length for $L_{SR}/2 < l < L_{SR}$, and frequency change is independent of the strained length for $l \geqslant L_{SR}$.

the whole strained length a few points from the unstrained section also contribute to the frequency response. Accordingly, it is expected that the DBSs registers less of a frequency response over these points than the applied strain that is shown as the flat maximum section in Fig. 3b. Scenario 3 is a special condition when none of the sampling points would register the Δv_B (applied strain) regardless of the location of the points with respect to the strained section, because the number of sampling points over the strained section is less than half the points covered by the spatial resolution window.

According to the conceptual representation of spatial resolution in Fig. 3, Ohsaki et al. [25] showed that the measured strain, ε_m, for a length shorter than L_{SR} can be linearly correlated with the applied strain, ε_a, through Eq. (3). However, as will be discussed in Section 3.2.1, the response of the DiTeSt™ for a strained length less than L_{SR} is different from what they concluded.

$$\varepsilon_m = l/L_{SR} \times \varepsilon_a \quad \text{for } l \le L_{SR} \tag{3}$$

3. Test results

3.1. Strain-free response of SMARTprofile™

As a first step, a 30 m long section of SMARTprofile™ cable is interrogated by the DiTeSt™ during almost 14 h resulting in 422 v_B measurement profiles along the cable while ΔT and $\Delta\varepsilon$ were zero. This is to quantify the noise level of the system below which any ΔT or $\Delta\varepsilon$ at any location along the cable cannot be discriminated from an unchanged section because of the presence of noise. This also allows quantification of the repeatability of the measurements and identification of eventual measurement drift, if any. The sensing cable configuration including the connection sequence of the sensors and DiTeSt™ is shown in Fig. 4. (ΔT during all tests presented in this paper was constant.)

3.1.1. Frequency spatial offset issues

Fig. 5 shows Brillouin frequency shift in GHz along the ε and T sensors length for all measurements before referencing with respect to the first measurement. Generally, there is a clear difference between v_B registered at the strain and temperature sensors because of the different embedment conditions of the sensors (Section 2.1). Also, being embedded in the PE jacket causes larger fluctuations in frequency measurements along the strain sensors than along the temperature sensors.

As stated in Section 2.1, variation in the Brillouin frequency shift is the parameter of interest to compute, thus all measurements must be referenced to the first measurement, i.e. the first measurement values are subtracted from all subsequent measurements in order to show changes. However, there are a number of outlier measurements where the DiTeSt™ registered completely wrong profiles along the entire cable which should be cleaned from the data before referencing. These outliers occurred along both strain and temperature sensors as well as connection fibers, although they are largely found as fluctuations in the strain sensors. These outliers mostly occurred when the system crashed for reasons such as extended runtime. These outliers are suppressed using a robust processing algorithm based on interquartile range (IQR) analysis [26].

In addition, it is noted that some measurements are offset relative to others along the horizontal axis. This offset is a location misalignment that occurs over the entire cable but it is more noticeable at the strain sensors, especially where there is a large difference in the Brillouin frequency shift, e.g. at the location where strain and temperature sensors meet (Fig. 5b). A probable reason for this misalignment is thought to be the 10 cm distance resolution of the system. This resolution is the ability of the system to detect the sampling point at its correct location along the cable so that a measurement at a point might be located either at its real position or within ±10 cm.

This issue along the sensing cable affects data referencing. An attempt was made to locally realign the measurements using a simple comparative algorithm based on the assumption that misalignment never exceeds one 10 cm distance sampling interval. As shown in Fig. 6, three frequency changes between the initial reading ($j = 1$) and subsequent readings ($j > 1$) for a point i and points before $(i-1)$ and after $(i+1)$ are considered and compared: $\Delta v_i = v_{i,j} - v_{i,1}$, $\Delta v_{i-1} = v_{i-1,j} - v_{i,1}$ and $\Delta v_{i+1} = v_{i+1,j} - v_{i,1}$. The smallest value of these three differences is considered

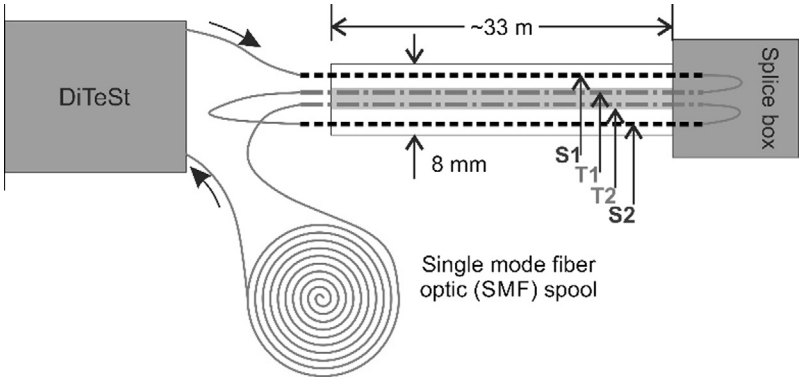

Fig. 4. DiTeSt™ and SMARTprofile™ connection status for the unstrained cable testing. There are two strain (S1–S2) and two temperature (T1–T2) sensors embedded in the SMARTprofile™.

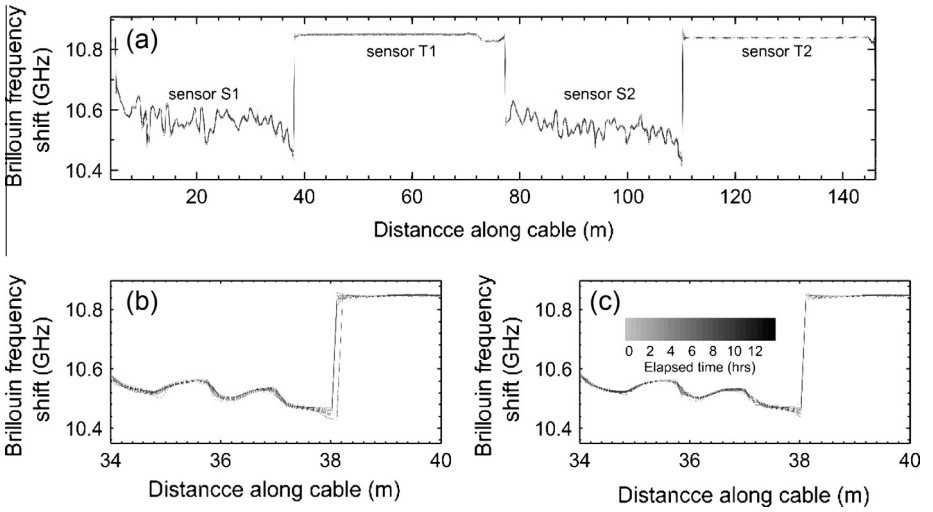

Fig. 5. (a) Over 400 registered Brillouin frequency shift profiles for strain sensors, (b) magnified view of the profile where S1 meets T1 showing a clear offset along the length and (c) the same profile shown in (b) after removing the offset issue.

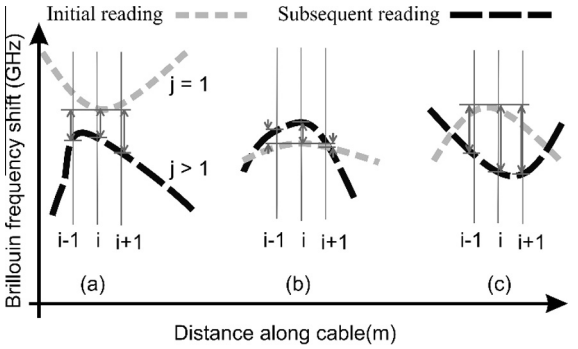

Fig. 6. Simple representation of the algorithm developed for reducing the spatial offset issue. Refer to text for (a), (b), and (c).

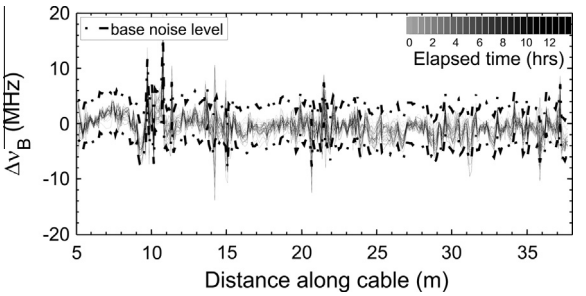

Fig. 7. Base noise interval of the processed Brillouin frequency shift change for sensor S1 to constrain the base noise level of the DiTeSt™.

as the more reliable, and the frequency shift readings are corrected accordingly: if $\Delta\nu_i$ is the smallest (Fig. 6a), $\nu_{i,j}$ is kept unchanged. If $\Delta\nu_{i-1}$ or $\Delta\nu_{i+1}$ are the smallest (Fig. 6b and c) then $\nu_{i,j} = \nu_{i-1,j}$ or $\nu_{i,j} = \nu_{i+1,j}$, respectively.

Fig. 5c shows the corrected original Brillouin frequencies after application of this algorithm; previously offset measurements are now aligned at their appropriate locations, resulting in better accuracy for later data analysis. It should be noted that this method has facilitated discrimination between unstrained sections and locally strained sections; therefore, it will not remove the real strain as an outlier.

3.1.2. Base noise level

The Brillouin frequency shifts are now corrected for outliers and misalignment issue. Referencing all measurements with the first measurement provides the relative Brillouin frequency shift, as shown in Fig. 7 for sensor S1, which brings ν_B data at each sampling point to almost zero. However, the $\Delta\nu_B$ data show fluctuations at all locations along the cable, so any small external ΔT or $\Delta\varepsilon$ in the cable would be masked if smaller than the noise level. In other words, the minimum physical change (ΔT, $\Delta\varepsilon$) applied to the cable must be above the noise level of the frequency profile in order to be detected as an anomaly along the cable.

From Fig. 7 it is noted that the frequency fluctuation at each point along the cable is different. Furthermore, because of the manufacturing process of the SMARTprofile™ cables, each shows dissimilar fluctuations at a particular point (distance along cable), so it is not possible to have the same standard deviation for a single point, e.g. at 5 m distance, for two different cables. Each point for every cable has its own standard deviation (SD), different from other points along the cables. Although it is possible to obtain such a noise level SD at each individual point, it might be time consuming. Rather a computed noise level based on the data recorded in this test can be used as an indicator of expected noise level for all SMARTprofile™ cables.

A simple statistical analysis was performed on the $\Delta\nu_B$ data at every point along cable (S1, S2, T1, and T2) in order to find the base noise level. Three standard deviations ($3 \times$ SD) for all points were stored in a matrix as a random variable. Then, the average of $3 \times$ SDs for all points along the cable was used to find a single, best $3 \times$ SD for the

entire cable, giving upper and lower bounds for the noise level, as shown with black dashed lines in Fig. 7, where this 3 × SD was added to and subtracted from the mean of the $\Delta\nu_B$ at each point, respectively.

The noise levels are summarized in Table 2 for all sensors. The correlation factors applied to $\Delta\nu_B$ to obtain $\Delta\varepsilon$ and ΔT are recommended by the DiTeSt™ manufacturer as 0.05055 MHz/με and 1.15 MHz/°C for ε and T sensors, respectively. It can be seen that strain variations due to noise are constrained to less than 160 με (∼±77 με).

3.2. Extensional test

In this section the DiTeSt™ response was evaluated when the sensing cable was longitudinally stretched (at constant T). The test was executed for different strained lengths, l, from 100 cm down to 1 cm. Displacement was applied to each strained length with 0.1 mm increments in order to induce a maximum 5000 με at the final step. Fig. 8 shows the test set-up and how the SMARTprofile™ cable was clamped and strained. Each clamp was an small aluminum block (1.5 cm wide, 5 cm long) containing a slot of dimension just under the cable cross-sectional area (4 × 8 mm) to ensure a good grip on the cable, as schematically shown in Fig. 8.

3.2.1. Linear correlation

Fig. 9a plots the relative Brillouin frequency shift change against distance along cable for all strained lengths, l, at the final displacement step, an applied 5000 με. A clear

Table 2
Base accuracy summary of the sensing cable.

Sensors		Strain sensors			Temperature sensors		
		S1	S2	Avg.	T1	T2	Avg.
Mean of 3 × SDs	Units						
	MHz	±3.6	±4.2	±3.9	±3.2	±2.9	±3.0
	με or °C	±71.3	±82.4	±76.9	±2.7	±2.5	±2.6

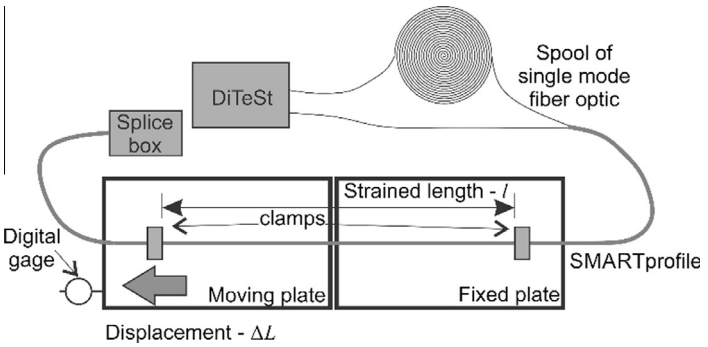

Fig. 8. SMARTprofile™ is clamped at both ends of the strained length, l, one on the fixed plate and the other on the moving plate.

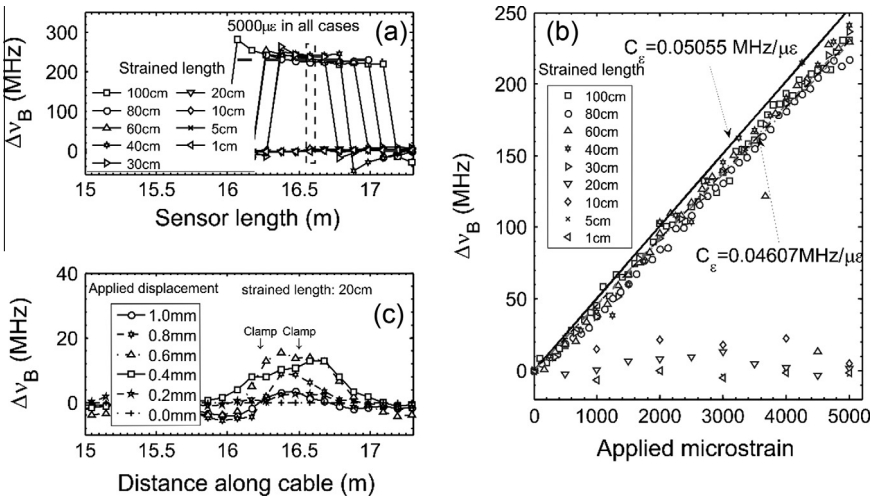

Fig. 9. (a) $\Delta\nu_B$ for application of 5000 με to various strained lengths, (b) best-fit correlation between applied strain and $\Delta\nu_B$ and (c) typical $\Delta\nu_B$ response applying incremental displacement to a 20 cm clamped length.

response was observed for all strained lengths above 25 cm, which is equal to half the spatial resolution, L_{SR}. For $l < L_{SR} = 50$ cm, it is expected from Section 2.2 that the frequency change response should be less than the applied microstrain. However, this effect was not observed and the $\Delta\nu_B$ for $l = 40$ and 30 cm was similar to that for $l \geqslant 50$ cm. However, it sometimes happened that the system could not detect any changes in the frequency profile for the 30 cm strained length.

On the other hand, no systematic $\Delta\nu_B$ is evident in Fig. 9a for all $l < 0.5 \times L_{SR}$, i.e. $l < 25$ cm, as explained in Section 2.2 and as confirmed by Glišić et al. [6]. Actually, an irregular response is observed; for example, for a 20 cm length $\Delta\nu_B$ initially increased slightly to less than 20 MHz for 0.6 mm tensioning followed by a drop with an increase in applied strain, Fig. 9c. Both of these issues are better understood in terms of the Brillouin gain spectrum, as discussed in Section 3.2.3.

As stated earlier, $\Delta\varepsilon$ and Brillouin frequency shift change are highly correlated. Fig. 9b plots $\Delta\nu_B$ at the middle of each strained section, indicated by the vertical dashed rectangle, versus the applied microstrain. The solid line represents the manufacturer's recommended correlation coefficient, i.e. $C_\varepsilon = 0.05055$ MHz/με; however, it tends to overestimate the measured $\Delta\nu_B$, particularly at high strains. Consequently, using all $\Delta\nu_B$ values for all strained lengths above $L_{SR}/2$, a new best-fit correlation was obtained as $C_\varepsilon = 0.04607$ MHz/με, the black dashed line in Fig. 9b, along with its 95% confidence interval, the light grey dashed lines.

3.2.2. Time-dependent behavior

In addition to tests described in Section 3.2.1, a 60 cm length of the cable was strained under 3 mm displacement over 15 h to assess time-dependent behavior. Fig. 10a and b shows the $\Delta\nu_B$ data against distance along cable and for the mid-point of the strained section. Measurements were quite repeatable during the straining period; they were confined within three standard deviation intervals of $\Delta\nu_B$ of only ±3.8 MHz, which is also consistent with the base noise level in the Section 3.1.2. This implies that the sensor in the strained section behaved independent of the time under strain, but this result contrasts with results from Valley et al. [27] where a constant dead load was used for stretching the cable and induced time-dependent behavior of $\Delta\nu_B$ over the test period. In this case a constant load boundary condition induced creep of the polyethylene cable, but in our case, with a constant displacement boundary condition, measurements are satisfactorily stable with time.

3.2.3. Short-length events

Section 3.2.1 showed that the frequency response over a strained length shorter than half the spatial resolution, $L_{SR}/2$, would not be detected by the system. Furthermore, the Brillouin frequency shift often shows a trough at points behind the clamps (Fig. 10a). Such behavior is better understood when considering the Brillouin gain spectrum, BGS (Fig. 2), as they can be attributed to the process of gain peak detection for strained lengths shorter than half the spatial resolution, hereafter called short-length events.

Fig. 11 shows the $\Delta\nu_B$ profile against distance along cable where a 50 cm length was stretched by 0.5 and 2.5 mm inducing 1000 με and 5000 με, respectively. Six points, denoted by 1–6, were considered for more detailed study of their BG spectra. At each sampling point the spatial resolution window covers $\pm L_{SR}/2$ before and after the point, therefore the spatial resolution window at points 1 and 6 was completely located within and outside the strained section, respectively. During two applied displacement steps, especially at higher displacements, the largest difference was observed between points 3 and 4, which were located just before and behind the right clamp, respectively. At the low displacement of 0.5 mm, a frequency change of almost 21 MHz was registered at point 4, similar to 31 MHz read for the point 3. However, at the higher displacement of 2.5 mm, the measured frequency change dropped to about 7 MHz for point 4, a significant difference with the 219 MHz registered at point 3 at the same step. This difference in the frequency of these two points at low and high displacements resulted from the curve fitting procedure of the system to the gain spectrum at each point, discussed below.

Brillouin gain spectrum is described by three components; the Brillouin frequency shift, ν_B, the full width at half maximum, *FWHM*, and the peak gain, g_B, i.e. Brillouin scattering coefficient (Fig. 1). When a uniform strain is applied along cable, the gain spectrum can be obtained using a Lorentzian fit based on Eq. (4) [28].

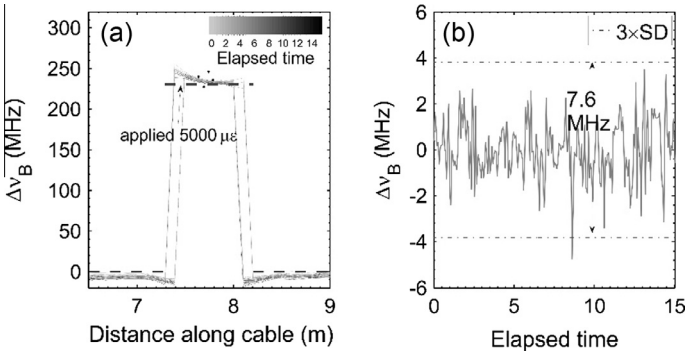

Fig. 10. (a) $\Delta\nu_B$ for application of 5000 με to a 60 cm strained length over 15 h and (b) $\Delta\nu_B$ for the mid-point of the strained length over time.

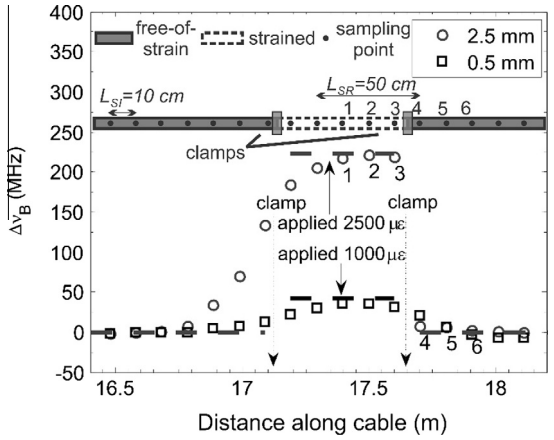

Fig. 11. Two different strain levels applied to a 50 cm strained length of SMARTprofile™; $\Delta\nu_B$ at six points 1–6 was considered for their different behavior at registration of Brillouin frequency at these two strain levels through study of Brillouin gain spectra in Fig. 12.

$$g(\nu_B) = (FWHM/2)^2 g_B / ((FWHM/2)^2 + (\nu - \nu_B)^2) \quad (4)$$

Fig. 12 shows the gain spectrum, various shaped dots, for the four sampling points indicated in Fig. 11 as points 1, 3, 4, and 6 for the two displacement steps as well as for the initial strain-free state of the cable. The Lorentzian fit for each gain spectrum at each point at the different displacements was drawn as a solid, and dashed–dotted curve in Fig. 12 for these three strain states. The spectrum for point 6, Fig. 12g–h, for all three displacement states remained unchanged with a peak gain at the frequency of the unstrained cable at this point. However, the spectrum associated with point 1 showed (Fig. 12a–b), apart from the unstrained state, two clear peaks with shifts in the frequency domain corresponding to each displacement state. Therefore a Lorentzian fit to each spectrum can be applied to detect the frequency at which the gain was maximized.

At the points 2–5 indicated in Fig. 11, the spatial resolution covered both unstrained and strained sections of the cable so that the gain spectrum for each displacement peaked at two locations, corresponding to the two sections. This gain spectrum can be considered as the sum of individual gain spectra of an unstrained and a strained length, $g_0(\nu) + g_\varepsilon(\nu)$, which are in the range of the spatial resolution (Fig. 13). Therefore the gain peaks without any shift in frequency for the non-strained section, whereas there would be a shift in frequency of the strained section relative to the amount of applied strain. Also, the gain peak of the strained section varies depending on the strained length, i.e. the shorter the length the smaller the peak. This is evident from comparing points 5–2, where the strained length increases from 10 to 40 cm.

Returning to points 3 and 4 in Fig. 12c–f, at low strains the peak gain of the strained section was hidden in the tail of the gain spectrum for the unstrained section. Therefore, a Lorentzian curve was fit to the spectrum which peaked at a frequency very close to the peak gain of the initial state. At higher applied strain, the peak gain in the strained section increased enough to be distinguished from the peak of the unstrained section, giving two individual peaks. However, the peak of the strained section decreased from point 3 to point 4 since the strained length decreased from 30 cm to 20 cm between these two points. At point 4, this caused the peak at the strained section to drop to values smaller than over the strain-free section. This variation in the length of the strained section from point 3 to point 4 resulted in peak gain detection at the frequency of the unstrained section as the final frequency, similar to Fig. 13b, whereas the largest of the two peaks at point 3 corresponded to the strained section, so the frequency of

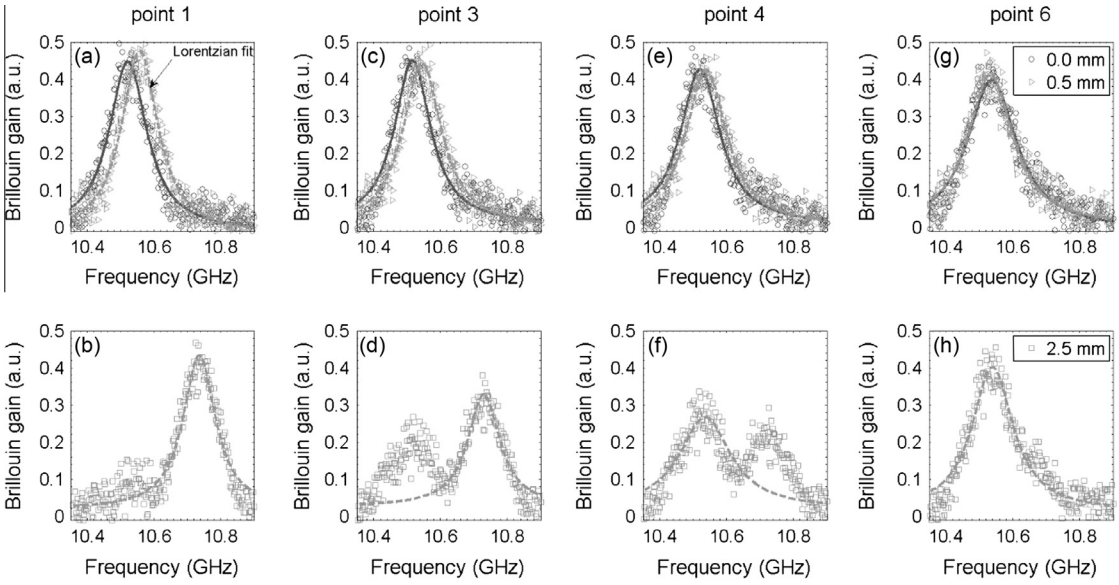

Fig. 12. Brillouin gain spectra for the six points shown in Fig. 11. Points 2–5 show two separate peaks at every displacement step corresponding to both strained and unstrained sections.

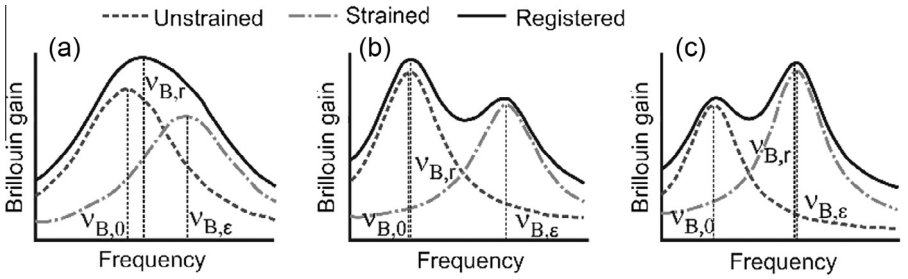

Fig. 13. Brillouin spectrum for a strained section when the applied strain (a) is lower than the critical strain, (b) is higher than critical strain but the strained section is shorter than unstrained length and (c) is higher than critical strain but the strained length is longer than unstrained section, modified from [29].

the strained section was estimated as the final measured frequency, as conceptually sketched in Fig. 13c and observed in Fig. 11.

An important finding is that the relative Brillouin frequency shift does not show measurable changes with different strained lengths less than L_{SR}, whereas the Brillouin gain factor shows such a dependency, i.e. it increases as the strained length increases up to the length of spatial resolution. In other words, in contrast to what Ohsaki et al. [25] showed, $\Delta\nu_B$ behaves independently of the strained length, as seen in Fig. 12, whereas $\Delta\nu_B$ remains constant for all points, although each point gives a spectrum peak of different magnitude. This explains why the system registered the $\Delta\nu_B$ profile for the lengths $L_{SR}/2 < l < L_{SR}$ shown in Fig. 9.

Another point worth noting is that at low strains, the amount of change in the Brillouin frequency shift is so limited that, particularly for short strained lengths, i.e. $<L_{SR}/2$, the peak gain of the strained portion of the cable becomes hidden in the peak gain related to the unstrained length (Fig. 13a). Researchers have considered different values for this strain limit including 1000 με [29] and 3000 με [30]. In this experimental study, the strain limit was evaluated to be at 2500 με, i.e. 1.25 mm for a 50 cm strained length.

The strain limit explains why the frequency profile over the strained length of the cable varies in its shape from a 'bell curve' at low strains to a 'boxcar' at high strains, specifically with respect to the Brillouin spectra at points 3 and 4. Fig. 14 shows such a transition for a 60 cm strained length of cable stretched up to 3 mm. The shape

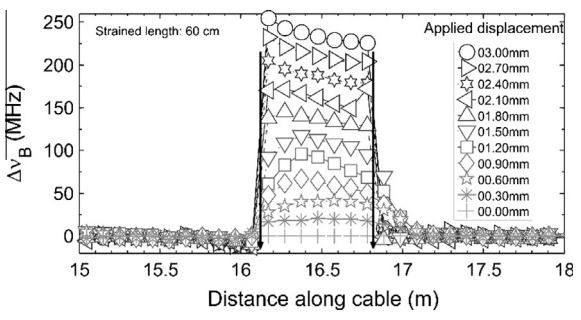

Fig. 14. Transition of $\Delta\nu_B$ profile from a bell curve shape at low strains to a boxcar shape at high strains. Two arrows show the locations of clamps.

conversion occurred at about 1.2 mm displacement, corresponding to 2500 με, as obtained from the Brillouin spectra shown in Fig. 12.

3.3. Lateral displacement

Understanding shear displacement in geomechanics studies is important, and the DBS has been used in a few application, e.g. to detect the sliding surface in failing natural slopes or embankments [31]. The displacement field in a rock mass includes various modes of deformation at different locations such as pure opening at joints or shearing along joint surfaces. Monitoring of a rock mass under shear displacement, particularly at long distances, can be extremely difficult due to the complex nature of shear displacement in comparison with tensile strain or joint opening. Therefore, it is of considerable interest if a monitoring system could address such a deformation mechanism. To explore the capability of the DiTeSt™ system under a shear displacement field, the sensing cable was subjected to a shear displacement. Various lengths of the sensing cable were clamped to the setup so that the cable was normal to the joint trace, as shown in Fig. 15.

The same test setup used for the extensional test was modified to accommodate lateral displacement applied normal to the clamped cable. It should be noted that the DiTeSt™ merely measures the axial strain whether the deformation is applied longitudinally or laterally. We expected the DBS to register a smaller frequency in the shear test configuration for the same strained length and displacement that were used in the tension test. Therefore, each strained length was sufficiently displaced laterally to induce a Brillouin frequency shift change of ~253 MHz to the cable, corresponding to an axial strain of 5000 με. According to a triangular approximation, a displacement almost 20 times more than the corresponding value in the extension test is then required.

The testing of the cable in this configuration resembled a model proposed by Newmark and Hall [32] for pipeline design under large displacements imposed by faults. In their model, the pipeline was assumed to be anchored at two symmetric locations at a distance of L_a ($L_a = l/2$) from a strike-slip fault trace where movement along the fault trace induced a tensile strain in the pipe, Fig. 16.

The total axial strain in the pipeline exposed to a lateral fault displacement is composed of an axial portion of the

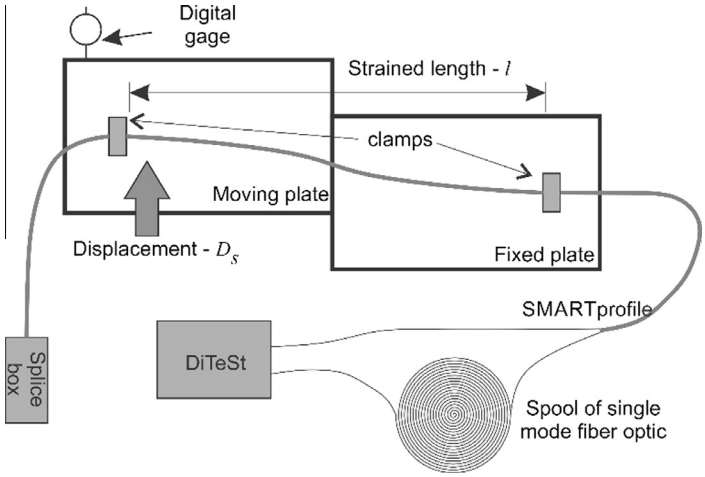

Fig. 15. A schematic view of the shear test setup along with the cable layout. Lateral displacement is applied normal to different strained lengths of cable.

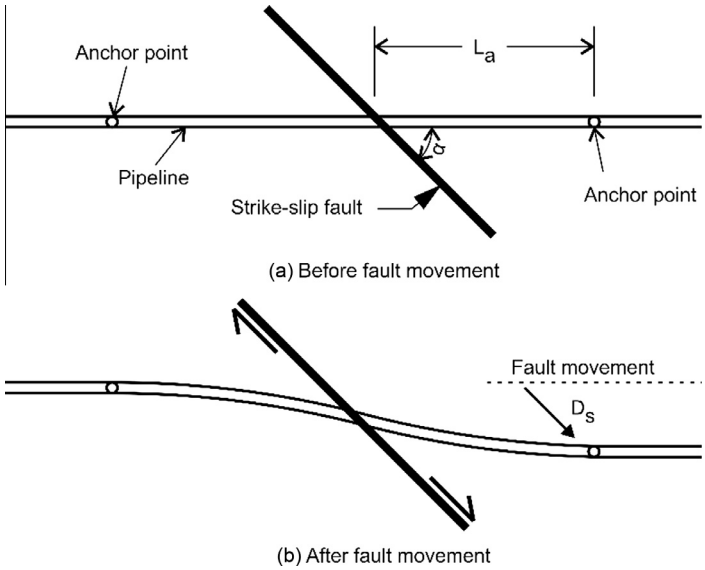

Fig. 16. Plan view of Newmark–Hall model for pipeline crossing a right lateral strike-slip fault. The pipe-fault relative inclination ($\alpha \leqslant 90°$) is in a way that fault movement induce tensile strain in the pipe with respect to the movement direction (modified from [32]).

fault movement ($D_S \cos\alpha$) and the arc-length effect induced by the lateral portion of the fault movement ($D_S \sin\alpha$), such that the average strain in the pipeline can be approximated as:

$$\bar{\varepsilon} = (D_S/2L_a)\cos\alpha + ((D_S/2L_a)\sin\alpha)^2/2 \quad (5)$$

In our test, because the direction of movement was normal to the cable longitudinal axis, α was 90°, then Eq. (5) was reduced to Eq. (6):

$$\bar{\varepsilon} = (D_S/2L_a)^2/2 \quad (6)$$

Fig. 17a shows the Brillouin frequency shift change versus applied strain during lateral displacement (computed from Eq. (6)) for the middle of the strained length. In general, it was found that DiTeSt™ could register the applied strain for all lengths down to 40 cm, although it sometimes happened that the system was even responsive for a 30 cm strained length. Furthermore, the induced $\Delta\nu_B$ over the strained length of the cable follows exactly the same linear correlation curve, i.e. 0.04607 MHz/με, as fit to the tension test results (see Section 3.2.1).

On the other hand, the Brillouin frequency shift change was plotted against the applied displacement for both axial and lateral displacement tests (Fig. 17b). While $\Delta\nu_B$ varied linearly with the applied displacement for the extension test, it followed a parabolic trend in the lateral displacement test, as expected from Eq. (6). It can be seen that in comparison with the tension test, a significantly larger displacement is required in order for the system to register a detectable frequency change in shear mode. This implies that the induced strain in the cable by arc-length effects

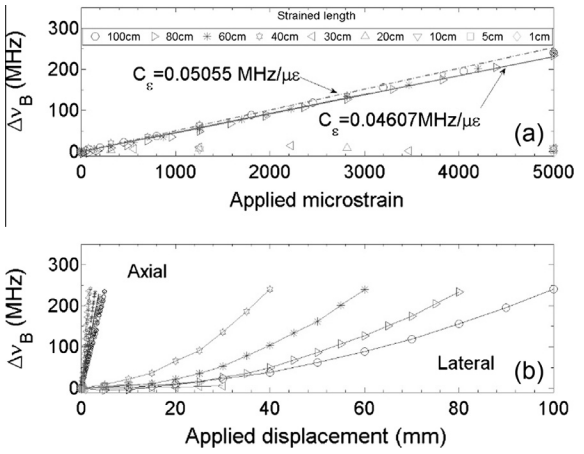

Fig. 17. Brillouin frequency shift change shows a linear correlation with applied microstrain in lateral displacement (a), while $\Delta\nu_B$ varies in a parabolic manner with the applied shear displacement in contrast to its linear correlation with the extensional displacement (b).

can be ignored. Therefore, small shear displacements might not be detected in the current cable-joint configuration until these displacements increase to much larger magnitudes, sufficient to be detected by the DiTeSt™.

Moreover, the parabolic trend of $\Delta\nu_B$–D_S profiles for the lateral displacement testing, Fig. 17b, could be used as an index to differentiate the shear along the joint surface rather than the joint opening at any location along the length of the cable, at least qualitatively. However, this distinctive behavior in $\Delta\nu_B$–D_S plots is most useful for the cable installed perpendicular to joints, since this diagnostic response will become less prominent as the angle α decreases from 90° to zero. This is due to a lesser contribution from arc-length effects in the average strain in the cable at smaller α values.

4. Conclusions

Distributed fiber optic sensors are useful in mining environments not only because of their durability and insensitivity to disturbing factors such as electromagnetic fields, moisture and noisy working areas, but also because of their capability of continuously measuring deformation at many points along their lengths as the size of the structure evolves. For example, a distributed optical cable installed in an appropriate configuration could continuously monitor rock mass strain as the size of a caving operation increases over a number of years. However, for successful technology application, confidence must be based on the actual response of such sensors under the conditions relevant for mine deformation monitoring. This article presented the results of a series of experimental tests on a DBS system to help understand the response to axial and shear displacements, what the limitations are, and how the results are to be interpreted.

Continuous interrogation of an unstrained SMARTprofile™ cable was performed to characterise the noise level below which no changes in temperature or deformation could be detected. Also, a spatial shift along cable was noticed from various overlain strain profiles, and this was partially corrected using a comparative algorithm. The results show that the system can provide high performance in strain sensing with a minimum noise level of ±75 με.

Extensional tests on various strained lengths show that the strain could be accurately detected down to a strained length above half the claimed spatial resolution, i.e. 25 cm. Below this length the registered response is unreliable, highlighting a system limitation for the measurement of short strained length sections. This limit also dictates the base requirement for future test designs and field installations (e.g. clamping points spacing). During these tests the frequency–strain conversion factor was re-evaluated and refined.

The behavior of deformation events over a strained length shorter than $L_{SR}/2$ is better understood when considering Brillouin gain spectra. It was found that $\Delta\nu_B$ changes are not linked to the strained length, but the peak gain can be correlated with the strained length.

When a sensing cable is exposed to a lateral movement, much larger displacement is required compared to a direct tension test in order to induce an equivalent strain in the cable. This is influenced by the relative angle between the displacement direction and the cable. While $\Delta\nu_B$ varied linearly with extensional displacement, it showed a parabolic variation with shear displacement, a distinctive response for this cable-joint configuration.

Acknowledgements

This work was funded by an equipment grant from NSERC (National Sciences and Engineering Research Council of Canada), CEMI (Centre for Excellence in Mining Innovation) by the Ontario Ministry of Research and Innovation through the SUMIT (Smart Underground Monitoring and Integrated Technology) research program.

References

[1] T. Horiguchi, M. Tateda, Optical-fiber-attenuation investigation using stimulated Brillouin scattering between a pulse and a continuous wave, Opt. Lett. 14 (1989) 408–410, http://dx.doi.org/10.1364/OL.14.000408.

[2] L. Thévenaz, M. Facchini, A. Fellay, M. Nikles, P. Robert, Field tests of distributed temperature and strain measurement for smart structures, 4th Pacific Rim Conf. Lasers Electro-Optics, 2001. CLEO/Pacific Rim 2001, IEEE, Chiba, Japan, 2001, pp. 490–491, http://dx.doi.org/10.1109/CLEOPR.2001.967938.

[3] D. Inaudi, B. Glišić, Distributed fiber optic strain and temperature sensing for structural health monitoring, in: IABMAS'06 3rd Int'l Conf. Bridg. Maintenance, Saf. Manag., Porto, Portugal, 2006, p. 8.

[4] D. Inaudi, B. Glišić, Integration of distributed strain and temperature sensors in composite coiled tubing, in: D. Inaudi, W. Ecke, B. Culshaw, K.J. Peters, E. Udd (Eds.), SPIE Proc. Vol. 6167 Smart Struct. Mater. 2006 Smart Sens. Monit. Syst. Appl., SPIE, San Diego, CA, 2006, p. 10, http://dx.doi.org/10.1117/12.661086.

[5] J. He, Z. Zhou, O. Jinping, Optic fiber sensor-based smart bridge cable with functionality of self-sensing, Mech. Syst. Signal Process. 35 (2012) 84–94, http://dx.doi.org/10.1016/j.ymssp.2012.08.022.

[6] B. Glišić, J. Chen, D. Hubbell, Streicker Bridge, A comparison between Bragg-grating long-gauge strain and temperature sensors and Brillouin scattering-based distributed strain and temperature sensors, in: M. Tomizuka (Ed.), Proc. SPIE 7981, Sensors Smart Struct. Technol. Civil, Mech. Aerosp. Syst., 2011, pp. 79812C–79812C–10, http://dx.doi.org/10.1117/12.881818.

[7] B. Glišić, D. Posenato, D. Inaudi, Integrity monitoring of old steel bridge using fiber optic distributed sensors based on Brillouin scattering, in: H.F. Wu, A.A. Diaz, P.J. Shull (Eds.), 14th Int. Symp. Smart Struct. Mater. Nondestruct. Eval. Heal. Monit., 2007, pp. 65310P–65310P–8, http://dx.doi.org/10.1117/12.716055.

[8] H. Murayama, K. Kageyama, Application of fiber-optic distributed sensors to health monitoring for full-scale composite structures, J. Intell. Mater. Syst. Struct. 14 (2003) 3–13, http://dx.doi.org/10.1177/1045389X03032738.

[9] S. Johansson, D. Watley, Dam safety experiences from distributed strain measurements in five embankment dams, Stockholm, Sweden, 2007.

[10] M. Iten, D. Hauswirth, A.M. Puzrin, Distributed fiber optic sensor development, testing and evaluation for geotechnical monitoring applications, in: W. Ecke, K.J. Peters, T.E. Matikas (Eds.), Proc. SPIE Vol. 7982 Smart Sens. Phenomena, Technol. Networks, Syst. 2011, San Diego, California, USA, 2011, pp. 798207–798207–15, http://dx.doi.org/10.1117/12.881228.

[11] H. Mohamad, P.J. Bennett, K. Soga, R.J. Mair, C.-S. Lim, C.K. Knight-Hassell, et al., Monitoring tunnel deformation induced by close-proximity bored tunneling using distributed optical fiber strain measurements, in: J. DiMaggio, P. Osborn (Eds.), 7th FMGM 2007 F. Meas. Geomech., American Society of Civil Engineers, Boston, Massachusetts, United States, 2007, pp. 1–13, http://dx.doi.org/10.1061/40940(307)84.

[12] H. Naruse, H. Uehara, T. Deguchi, K. Fujihashi, M. Onishi, R. Espinoza, et al., Application of a distributed fibre optic strain sensing system to monitoring changes in the state of an underground mine, Meas. Sci. Technol. 18 (2007) 3202–3210, http://dx.doi.org/10.1088/0957-0233/18/10/S23.

[13] X. Zeng, X. Bao, C.Y. Chhoa, T.W. Bremner, A.W. Brown, M.D. DeMerchant, et al., Strain measurement in a concrete beam by use of the Brillouin-scattering-based distributed fiber sensor with single-mode fibers embedded in glass fiber reinforced polymer rods and bonded to steel reinforcing bars, Appl. Opt. 41 (2002) 5105–5114.

[14] C. Lan, Z. Zhou, J. Ou, Full-scale prestress loss monitoring of damaged RC structures using distributed optical fiber sensing technology, Sensors (Basel) 12 (2012) 5380–5394, http://dx.doi.org/10.3390/s120505380.

[15] J.-M. Henault, M. Quiertant, S. Delepine-Lesoille, J. Salin, G. Moreau, F. Taillade, et al., Quantitative strain measurement and crack detection in RC structures using a truly distributed fiber optic sensing system, Constr. Build. Mater. 37 (2012) 916–923, http://dx.doi.org/10.1016/j.conbuildmat.2012.05.029.

[16] L. Zou, G.a. Ferrier, S. Afshar, Q. Yu, L. Chen, X. Bao, Distributed Brillouin scattering sensor for discrimination of wall-thinning defects in steel pipe under internal pressure, Appl. Opt. 43 (2004) 1583–1588.

[17] F. Bastianini, M. Cargnelutti, A. Di Tommaso, M. Toffanin, Distributed Brillouin fiber optic strain monitoring applications in advanced composite materials 5057 (2003) 478–485, http://dx.doi.org/10.1117/12.482392.

[18] X. Li, B.P. America, T. Parker, M. Farhadiroushan, D. Blacklaw, Evaluating a concept of using distributed optical fiber temperature and strain sensor for continuous monitoring of casing and completion mechanical deformation, in: Offshore Technol. Conf., 2004, pp. 1–17.

[19] Noni, M.M. MacLaughlin, H.F. Wang, Validation of fiber-optic strain-sensing cable for deep underground installation, in: 45th US Rock Mech./Geomech. Symp., 2011, p. 10.

[20] P.K. Kaiser, P. Vasak, F.T. Suorineni, D. Thibodeau, New dimensions in seismic data interpretation with 3-D virtual reality visualization for burst-prone mines, in: Y. Potvin, M. Hudyma (Eds.), 6th Int. Symp. Rockburst Seism. Mines, Australian Centre for Geomechanics, Perth, Australia, 2005, pp. 33–45.

[21] S. Adachi, Distributed optical fiber sensors and their applications, in: SICE Annu. Conf. 2008, Tokyo, Japan, 2008, pp. 329–333, http://dx.doi.org/10.1109/SICE.2008.4654674.

[22] D. Inaudi, Application of Fiber Optic Sensors to Structural Monitoring, 4763 (2003) 31–38, http://dx.doi.org/10.1117/12.508669.

[23] L. Thévenaz, Brillouin distributed time-domain sensing in optical fibers: state of the art and perspectives, Front. Optoelectron. China 3 (2010) 13–21, http://dx.doi.org/10.1007/s12200-009-0086-9.

[24] L. Thévenaz, M. Nikles, A. Fellay, M. Facchini, P.A. Robert, Applications of distributed Brillouin fiber sensing, in: P.K. Rastogi; F. Gyimesi (Eds.), Proc. SPIE 3407, Int. Conf. Appl. Opt. Metrol. 374, International Society for Optics and Photonics, Balatonfured, Hungary, 1998, pp. 374–381, http://dx.doi.org/10.1117/12.323342.

[25] M. Ohsaki, M. Tateda, T. Omatsu, Spatial resolution enhancement of distributed strain measurement using BOTDR by partially gluing optical fiber, IEICE Trans. Commun. 85 (2002) 1636–1639.

[26] D. Posenato, P. Kripakaran, D. Inaudi, I.F.C.C. Smith, Methodologies for model-free data interpretation of civil engineering structures, Comput. Struct. 88 (2010) 467–482, http://dx.doi.org/10.1016/j.compstruc.2010.01.001.

[27] B. Valley, B.M. Madjdabadi, P.K. Kaiser, M.B. Dusseault, Monitoring mining-induced rock mass deformation using distributed strain monitoring based on fiber optics, in: Eur. Rock Mech. Symp. 2012, International Society for Rock Mechanics, Stockholm, Sweden, 2012, p. 14.

[28] H. Murayama, K. Kageyama, H. Naruse, A. Shimada, Distributed strain sensing from damaged composite materials based on shape variation of the Brillouin spectrum, J. Intell. Mater. Syst. Struct. 15 (2004) 17–25, http://dx.doi.org/10.1177/1045389X04039263.

[29] H. Zhang, Z. Wu, Performance evaluation of BOTDR-based distributed fiber optic sensors for crack monitoring, Struct. Health Monit. 7 (2008) 143–156, http://dx.doi.org/10.1177/1475921708089745.

[30] M. Iten, A.M. Puzrin, BOTDA road-embedded strain sensing system for landslide boundary localization, in: N.G. Meyendorf, K.J. Peters, W. Ecke (Eds.), Proc. SPIE 7293, Smart Sens. Phenomena, Technol. Networks, Syst. 2009, San Diego, California, USA, 2009, pp. 729316–729316–12, http://dx.doi.org/10.1117/12.815266.

[31] M. Iten, Novel applications of distributed fiber-optic sensing in geotechnical engineering, PhD thesis, ETH Zurich, 2011.

[32] N.M. Newmark, W.J. Hall, Pipeline design to resist large fault displacement, in: Proceedings, 1s US Natl. Conf. Earthq. Eng., Earthquake Eng. Res. Inst., Ann Arbor, Michigan, 1975, pp. 416–425.